

A 3D dynamical model of the colliding winds in binary systems

E. R. Parkin[★] and J. M. Pittard

School of Physics and Astronomy, the University of Leeds, Leeds LS2 9JT

Accepted 2008 May 21. Received 2008 May 20; in original form 2008 April 22

ABSTRACT

We present a three-dimensional (3D) dynamical model of the orbital-induced curvature of the wind–wind collision region in binary star systems. Momentum balance equations are used to determine the position and shape of the contact discontinuity between the stars, while further downstream the gas is assumed to behave ballistically. An Archimedean spiral structure is formed by the motion of the stars, with clear resemblance to high-resolution images of the so-called ‘pinwheel nebulae’. A key advantage of this approach over grid or smoothed particle hydrodynamic models is its significantly reduced computational cost, while it also allows the study of the structure obtained in an eccentric orbit. The model is relevant to symbiotic systems and γ -ray binaries, as well as systems with O-type and Wolf–Rayet stars.

As an example application, we simulate the X-ray emission from hypothetical O+O and WR+O star binaries, and describe a method of ray tracing through the 3D spiral structure to account for absorption by the circumstellar material in the system. Such calculations may be easily adapted to study observations at wavelengths ranging from the radio to γ -ray.

Key words: hydrodynamics – methods: numerical – binaries: general – stars: early-type – stars: winds, outflows – X-rays: stars.

1 INTRODUCTION

Colliding winds occur in various types of stellar binaries, including those with massive OB and Wolf–Rayet (WR) stars, lower mass eruptive symbiotic systems containing a white dwarf and red giant star which undergo a ‘slow nova’ outburst and binary systems which contain one or two pulsars blowing a pulsar wind(s).

High-spatial-resolution observations are revealing many interesting features in such systems. In massive O+O and WR+O binaries, radio interferometry has spatially resolved emission from non-thermal electrons at the apex of the wind–wind collision (e.g. Williams et al. 1997; Dougherty, Williams & Pollacco 2000; Contreras, Montes & Wilkin 2001; Dougherty et al. 2005). Beautiful ‘pinwheel’ structures which trace dust emission can also be observed (e.g. Monnier, Tuthill & Danchi 1999; Tuthill, Monnier & Danchi 1999; Marchenko et al. 2002; Tuthill et al. 2006, 2008). The shape of these structures can be described by Archimedean spirals which are believed to follow the wind–wind collision region in systems where the winds are of very unequal momentum.

Colliding winds also play a key role in eruptive symbiotic systems, where a hot, fast, diffuse wind from a white dwarf companion

interacts with a slow massive wind from a Mira-type primary star.¹ The class of eruptive symbiotics can be divided into two further subtypes: classical symbiotics, in which the bolometric luminosity remains constant and outbursts typically last about 100 d (Z And is an example), and the more powerful eruptions known as symbiotic novae, where the bolometric luminosity increases by a factor of order 10–100 on a time-scale of about a year, and the system stays in an active state for $\gtrsim 10$ yr (well-known examples are V1016 Cyg, HM Sge and AG Pegasi).

Colliding winds may also play a key role in the newly discovered class of systems called γ -ray binaries (Aharonian et al. 2005a,b; Albert et al. 2006). The nature of these systems is still controversial, though in the case of PSR B1259–63, it is clear that a relativistic wind from a pulsar collides with the stellar wind from a Be star. The orbit is highly eccentric ($e = 0.87$), and has a period of 3.4 yr (Johnston et al. 2005). The TeV γ -ray emission arises from the inverse Compton cooling of ultrarelativistic electrons accelerated at the pulsar wind termination shock (e.g. Khangulyan et al. 2007).

¹ Such systems are to be distinguished from the interacting wind phenomenon which occurs in asymptotic giant branch (AGB) binaries where density structures in the AGB wind are created either due to the reflex action of the evolved star around the centre of mass of the system (Mastrodemos & Morris 1999; Mauron & Huggins 2006; He 2007), or due to gravitational focusing (Gawryszczak, Mikołajewska & Rozycka 2002). Here we focus exclusively on systems involving the interaction of winds from separate stars.

[★]E-mail: phy1erp@leeds.ac.uk

In contrast, the nature of the sources LS5039 and LSI+61 303 is less clear, since the type of compact object has not been established beyond doubt (Romero et al. 2007; Dubus, Cerutti & Henri 2008; Khangulyan, Aharonian & Bosch-Ramon 2008).

While there has been much progress in modelling the dynamical structure of the colliding winds in early-type binary systems, the majority of work has been limited to two-dimensional (2D; e.g. Stevens, Blondin & Pollock 1992; Gayley, Owocki & Cranmer 1997; Pittard et al. 1997; Pittard 1998, 2007; Zhekov 2007). Three-dimensional (3D) hydrodynamical calculations have been performed by Pittard (1999), Walder & Folini (2002) and Lemaster, Stone & Gardiner (2007), while a ballistic model was presented by Harries et al. (2004). A smoothed particle hydrodynamics (SPH) model has recently been computed by Okazaki et al. (2008). Dynamical models for symbiotic novae have been presented by Girard & Willson (1987) and Kenny & Taylor (2005, 2007), while 3D hydrodynamical models have been presented by Walder & Folini (2000). Models of the wind–wind collision in classical symbiotics have been presented by Mitsumoto et al. (2005) and Bisikalo et al. (2006). Relativistic hydrodynamics (Bogovalov et al. 2008) and SPH (Romero et al. 2007) models have been used to investigate the wind–wind collision in pulsar wind binary systems.

Although dramatic improvements in computational power and techniques in recent years have spurred the development of 3D models of colliding winds, such work remains computationally expensive, and it is still difficult to perform simulations of colliding wind binaries even on high performance parallel machines when the orbital eccentricity is high. We therefore present a new method which captures the flow dynamics while requiring less computational resources.

At its heart, our approach adopts the equations for the ram pressure balance between the two winds as detailed by Canto, Raga & Wilkin (1996). In this work it is assumed that both winds are highly radiative, rapidly cool and fully mix. While these assumptions are only relevant in close binaries, it provides a convenient starting point and the position of the contact discontinuity (CD) is unlikely to drastically change even if the wind–wind collision is essentially adiabatic. Then, at some distance downstream of the apex of the wind–wind collision region the flow is assumed to reach a terminal speed and to thereafter flow ballistically (i.e. no net force acting upon it). This ballistic treatment has similarities to many previous works (e.g. Girard & Willson 1987; Harries et al. 2004; Kenny & Taylor 2007). The derivation in Canto et al. (1996) has also been widely used to model observable properties (e.g. Foellmi et al. 2008; Henley et al. 2008).

This paper is organized as follows. In Section 2 we explain the steps necessary to construct our dynamical model of the wind–wind collision. Section 3 shows how it can be used to simulate the X-ray emission and circumstellar absorption arising from the wind collision region (WCR) in early-type binary systems, though this is but one example of the potential use of such a model. In Section 4 we summarize and conclude our findings, and outline possible future directions.

2 THE DYNAMICAL MODEL

2.1 Overview

In the model the orbit is calculated in the frame of one of the stars (hereafter referred to as the primary star). The winds are assumed to reach their terminal speeds before they collide. The CD is split into two sections to account for the effect of orbital motion.

(i) A region close to the apex of the WCR where the flow from the stagnation point is accelerating along the CD (hereafter called the ‘shock cap’). The shock cap is terminated where the flow is assumed to become ballistic (the ‘ballistic point’), the exact point being calibrated against hydrodynamical models (see Section 2.3). While the properties of the shock cap are assumed to be axisymmetric, orbital motion introduces an aberration angle which means that the symmetry axis and the line of centres of the stars are not collinear (see Section 2.2).

(ii) A region beyond the ballistic point where the flow along the CD is unaffected by the primary and secondary stars’ gravity, ram pressure from the winds or thermal pressure in the WCR. If the stellar winds have differing speeds, the flow in this region is assumed to move with the speed of the slower wind, since this is the wind which responds least to the orbital motion of the stars, and dominates the absorption in the system (in the models presented in this paper, both winds have the same speed of 2000 km s^{-1} – see Table 2). This region is termed the ‘ballistic CD’.

By separating the CD into these two sections we can model the effect of the winding of the CD around the stars and the subsequent absorption by the unshocked winds. We do not attempt to model the shocks which bound either side of the CD in this work, as in many circumstances the shocked gas efficiently cools and is compressed by the ram pressure of the pre-shock wind into a thin dense sheet coincident with the CD. For instance, in symbiotic novae, the hot wind is likely to be strongly radiative (see fig. 4 in Kenny & Taylor 2005), as of course is the cool wind, and our model therefore gives the position of the shocked gas and the dense spiral shells which subsequently form. Strong radiative cooling is also a feature of the WCR in many massive binaries. In η Car, for example, the primary luminous blue variable (LBV) wind is so dense (and slow) that it is strongly radiative around the entire orbit (Pittard et al. 1998). The importance of cooling in the WCR can be quantified using the cooling parameter (Stevens et al. 1992),

$$\chi = \frac{t_{\text{cool}}}{t_{\text{esc}}} = \frac{v_8^4 d_{12}}{\dot{M}_7}, \quad (1)$$

where v_8 is the wind velocity in units of 1000 km s^{-1} , d_{12} is the separation of the stars in units of 10^{12} cm , \dot{M}_7 is the mass-loss rate of the star in units of $10^{-7} M_{\odot} \text{ yr}^{-1}$, t_{cool} is the cooling time and $t_{\text{esc}} (= d/c_s, c_s$ is the post-shock sound speed) is the characteristic time for hot gas near the apex of the WCR to flow downstream. In practice, hydrodynamical simulations show that the WCR is adiabatic for $\chi \gtrsim 3$, whereas for $\chi \lesssim 3$ it cools rapidly (Fig. 1).

Fig. 2 shows the value of χ as a function of orbital period for each shocked wind in a hypothetical O+O star binary with a circular orbit, wind speeds of 2000 km s^{-1} and mass-loss rates of 10^{-6} and $2 \times 10^{-7} M_{\odot} \text{ yr}^{-1}$ for the primary and secondary star of masses 50 and $30 M_{\odot}$, respectively. Clearly, both of the shocked winds are largely adiabatic, even down to an orbital period of 10 d (in shorter period systems the stars are close enough together that acceleration/deceleration of the winds needs to be considered). However, in a hypothetical WR+O system where the mass-loss rates of the primary and secondary stars are now 2×10^{-5} and $10^{-6} M_{\odot} \text{ yr}^{-1}$, and both stars have masses of $50 M_{\odot}$ and wind speeds of 2000 km s^{-1} , cooling is important for orbital periods $\lesssim 1 \text{ yr}$. If the WR star is a WC subtype, cooling is important for periods up to several years, since cooling is more efficient with such abundances (see e.g. Stevens et al. 1992). Thus, Fig. 2 shows that the denser winds from WR stars are likely to produce radiative shocks in many instances, though the O+O systems will usually be adiabatic unless the orbital period,

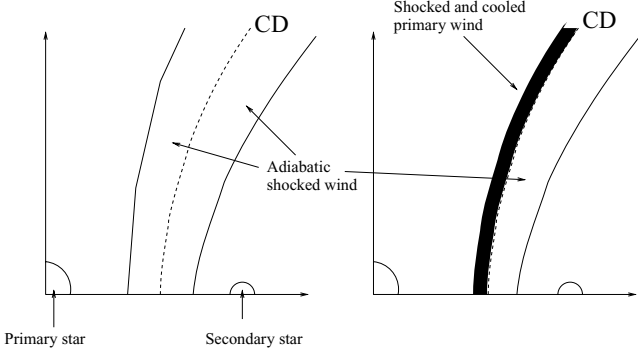


Figure 1. Schematic diagram showing the location of the shocks bounding the CD for varying values of the cooling parameter. Left: both winds have $\chi \gtrsim 1$ and are therefore largely adiabatic. Right: the primary wind has $\chi \ll 1$ and is strongly radiative, whereas the secondary wind is adiabatic. The scenario on the left represents the O+O and WR+O binaries investigated in this paper, whereas the scenario on the right represents what is thought to occur in η Car.

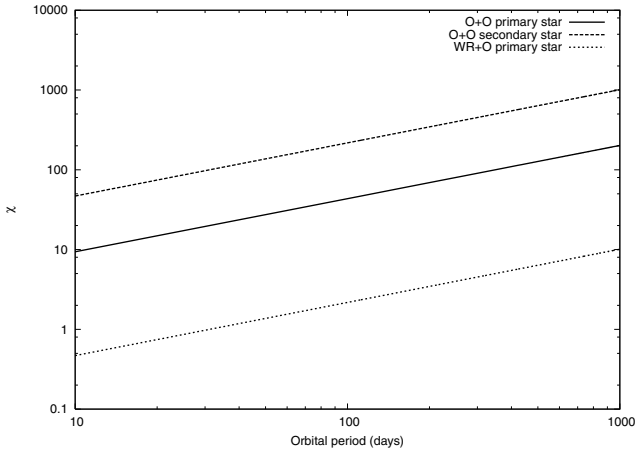


Figure 2. Ratio of the cooling to characteristic flow time-scale for the hot shocked gas in a colliding winds binary as a function of orbital period. Cooling becomes important once $\chi \lesssim 3$.

$P \lesssim 10$ d, or the winds are slower and/or denser than assumed above.

The post-shock winds of both the primary and secondary stars in the simulations discussed in Section 3 are largely adiabatic. In such cases, the temperature of the hot gas in the WCR as a function of distance downstream from the stagnation point at the apex of the WCR has been determined by Kenny & Taylor (2005). With this information it is possible to derive the width of the post-shock layer, and hence the position of the shocks, as a function of downstream distance. However, this is beyond the scope of the present work.

In the following sections we detail the modelling of the shock cap and ballistic CD.

2.2 The shock cap

The shape of the shock cap is determined from momentum balance requirements. The surface density and velocity of the flow along the shock cap are obtained from equations (29) and (30) of Canto et al. (1996) (the latter scaled to the speed of the slower wind). Assuming

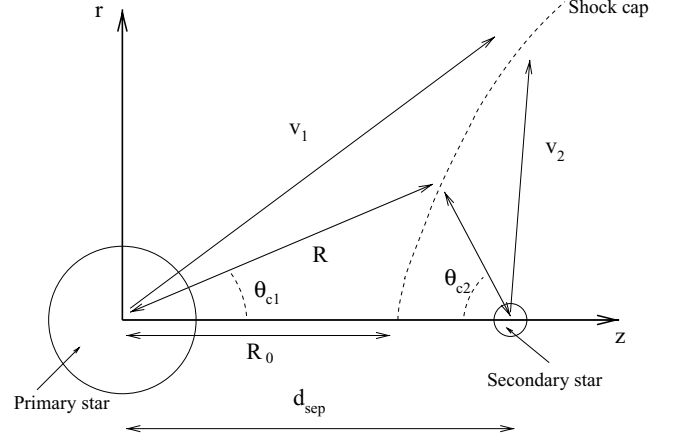


Figure 3. Schematic diagram describing the wind–wind interaction between the two stars represented by circles.

the winds are already at their terminal velocity when they reach the shocks, the locus of the CD is $R(\theta_{c1})$, where R is the distance from the centre of the primary star and θ_{c1} is the angle between the vector to the primary star and the line-of-centres (see Fig. 3). The ratio of the wind momenta is given by

$$\eta \equiv \frac{\dot{M}_2 v_{\infty 2}}{\dot{M}_1 v_{\infty 1}}, \quad (2)$$

where \dot{M}_1 , $v_{\infty 1}$, \dot{M}_2 and $v_{\infty 2}$ are the mass-loss rates and terminal velocities of the primary and secondary stars, respectively.

The shock cap is symmetrical about the line of centres before the effects of orbital motion are introduced. The 2D (r, z) coordinates of points on the shock cap in units of the stellar separation, d_{sep} , are

$$z = \frac{\tan \theta_{c1}}{\tan \theta_{c2} + \tan \theta_{c1}}, \quad (3)$$

$$r = z \tan \theta_{c2}. \quad (4)$$

To determine the coordinates in 3D, the 2D arms of the WCR can be rotated azimuthally. The x , y and z vectors (x_{cap} , y_{cap} and z_{cap} , respectively) from the centre of the primary star to coordinates on the shock cap are then

$$x_{cap} = d_{sep}(z \cos \omega - r \sin \omega \cos \zeta),$$

$$y_{cap} = d_{sep}(z \sin \omega + r \cos \omega \cos \zeta),$$

$$z_{cap} = d_{sep}(r \sin \zeta),$$

where ω is the true anomaly of the orbit and ζ is the azimuthal angle subtended between a coordinate on the surface of the shock cap, the line of centres and the xy (orbital) plane.

The number of coordinate points on the shock cap is determined by the values of $\theta_{c1\infty}$, $\delta\theta_{c1}$ and $\delta\zeta$. With $\delta\theta_{c1} = 1^\circ$ and $\delta\zeta = 18^\circ$ (i.e. 20 azimuthal points per 2D rz value), the shock cap consists of $\sim 10^3$ separate coordinate points. equation (29) of Canto et al. (1996) is used to determine the tangential velocity along the CD, and thus the position of the ballistic point in 2D axisymmetry.

Since the size of the wind–wind collision scales with the orbital separation, dramatic variations occur in systems with highly eccentric orbits, as shown in Fig. 4 where $e = 0.9$; the high eccentricity means that the shock cap at periastron has a linear scale which is 20 times smaller than that at apastron. Such high eccentricities occur

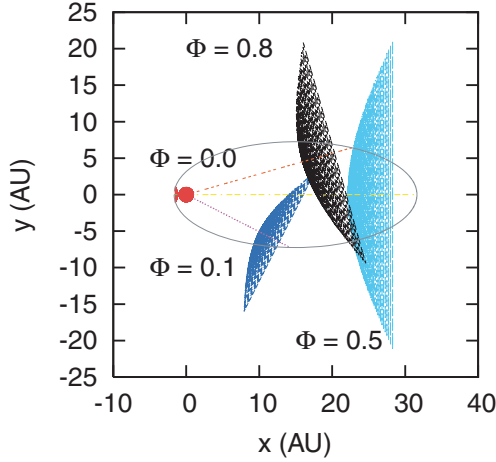


Figure 4. Plan view of the shock cap at various orbital phases in a system with an orbital eccentricity, $e = 0.9$. The calculations are performed in the frame of the primary star (located at the origin and not to scale) with the secondary star orbiting in an anticlockwise direction. As the separation of the stars increases the linear size of the shock cap also increases in direct proportion. This is most noticeable when comparing the shock cap at $\phi = 0.0$ (periastion, red) and $\phi = 0.5$ (apastron, turquoise). The aberration (skew) of the shock cap due to orbital motion is not considered in this plot.

in two of the most well known colliding winds systems, η Car and WR 140, and also in PSR B1259–63, one of the γ -ray binaries.

Another effect resulting from orbital motion is the aberration (skew) of the apex of the WCR due to the net velocity vector of the orbit (i.e. the motion of the secondary star relative to the primary star). The skew angle, μ , which is the angle between the symmetry axis of the shock cap and the line of centres of the stars is approximated by

$$\tan \mu = \frac{v_{\text{orb}}}{v_{\infty}}, \quad (5)$$

where the speed of the slower wind is used. In the frame of the primary star,

$$v_{\text{orb}} = \left[G(M_1 + M_2) \left(\frac{2}{d_{\text{sep}}} - \frac{1}{a} \right) \right]^{1/2} \quad (6)$$

for stars of mass M_1 and M_2 and an orbital semimajor axis, a .

The aberration is significant in symbiotic novae because of the low wind speed of the cool star (for instance, a symbiotic system with $e = 0.0$, $M_1 + M_2 = 2.5 M_{\odot}$ and $d_{\text{sep}} = 10$ au has $v_{\text{orb}} = 15 \text{ km s}^{-1}$, which is comparable to the speed of the cool wind). In contrast, the aberration is small in early-type binaries (for instance, an O+O binary with $e = 0.0$, $M_1 + M_2 = 80 M_{\odot}$ and $d_{\text{sep}} = 4.3$ au has $v_{\text{orb}} = 130 \text{ km s}^{-1}$, which is typically much smaller than the wind speeds), unless the orbit has high eccentricity. In such cases the magnitude of the skew varies throughout the orbit.

Fig. 5 shows how μ varies throughout the orbit for the model A O+O star binary with parameters as in Table 2 and with $e = 0.3$ and 0.9 . A peak value is reached at periastron passage ($\phi = 0.0$) when the relative orbital speed of the stars reaches its highest value, and the lowest value of μ occurs when the stars are at apastron ($\phi = 0.5$) and the relative orbital velocity is a minimum. The variation of μ between apastron and periastron increases with the eccentricity of the orbit. The skew angle μ can affect the proximity of regions of the shock cap to the primary star around periastron (Fig. 6), and the resulting level of occultation and attenuation.

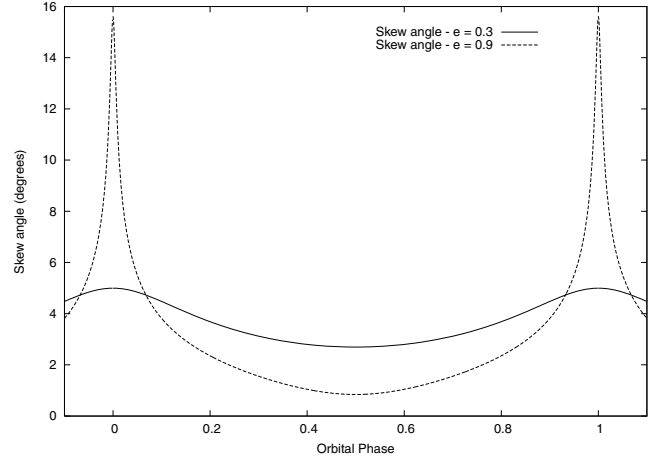


Figure 5. Variation of the skew angle of the shock cap due to orbital motion for eccentricities of $e = 0.3$ and 0.9 , with $P = 1$ yr and $M_1 + M_2 = 80 M_{\odot}$. The angle peaks at phase $\phi = 0.0$, when the stars are at closest approach and their relative orbital velocity is a maximum.

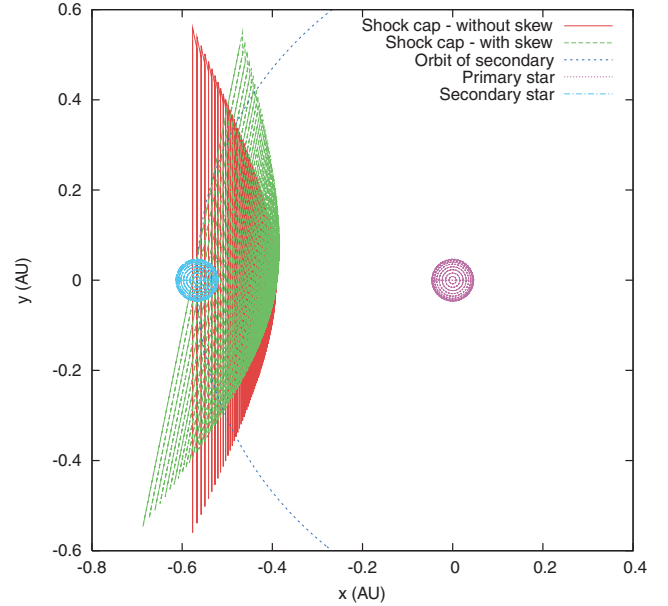


Figure 6. Plan view of the shock cap at $\phi = 0.0$ for $e = 0.9$, $P = 1$ yr and $M_1 + M_2 = 80 M_{\odot}$, with (green) and without (red) taking account of orbit-induced skew. The secondary star orbits in the anticlockwise direction. Note that the shocks either side of the CD are not displayed.

2.3 The ballistic CD

To construct the large-scale 3D structure of the WCR, gas packets are released from the endpoints of the shock cap at specific phase intervals with a velocity equal to the slower wind, v_{sl} . The x , y and z components of the velocity of gas leaving the end of the shock cap at a specific orbital phase are given by

$$\hat{v}_x = v_{\text{sl}} \cos(\omega - \mu + \lambda \cos \zeta),$$

$$\hat{v}_y = v_{\text{sl}} \sin(\omega - \mu + \lambda \cos \zeta),$$

$$\hat{v}_z = v_{\text{sl}} \sin \zeta,$$

where $\lambda = \theta_{\text{c1}\infty}$ is the asymptotic half-opening angle of the CD viewed from the star with the stronger wind.

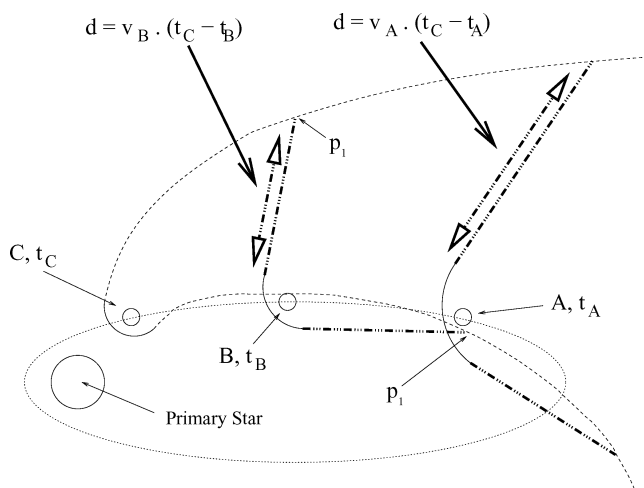


Figure 7. Schematic diagram showing how position vectors to points on the ballistic CD are obtained. If the secondary star is currently at position C, points p_1 on the ballistic CD are found by determining the position and flow direction of gas leaving the end of the shock cap when the star is at position B and advecting the flow by the time difference between these two orbital phases. This process is repeated until the position of the ballistic CD has been traced back the desired number of orbits (in this work the structure is traced back over two orbits). Distances of 100–1000 au can easily be covered, as required.

The ballistic part of the CD is then constructed by considering a sequence of previous positions of the ballistic points at the termination of the shock cap, and the current position of the gas flow from these points given that they move along linear trajectories (see Fig. 7).

The position of points on the ballistic part of the CD (x_{CD} , y_{CD} and z_{CD}) at the time t is given by their position at the time they were emitted from the end of the shock cap (x_{cap} , y_{cap} and z_{cap}) plus the distance they have since travelled at velocity \hat{v}_x , \hat{v}_y , \hat{v}_z , i.e.

$$x_{CD}(t) = x_{cap}(t - T) + \hat{v}_x(t - T)T,$$

$$y_{CD}(t) = y_{cap}(t - T) + \hat{v}_y(t - T)T,$$

$$z_{CD}(t) = z_{cap}(t - T) + \hat{v}_z(t - T)T,$$

where T is the time elapsed since the flow left the end of the shock cap.

The number of coordinates in the ballistic CD is dependant on the number of phase steps around the orbit, the number of orbital revolutions followed and the number of azimuthal steps (i.e. $\delta\zeta$). In this work, the ballistic CD consists of 2000 coordinate positions along each azimuthal trajectory (1000 per orbit traced).

Tests performed using a 3D hydrodynamics code confirm that the Coriolis force, which causes the curvature to the WCR, becomes significant once the flow from the stagnation point is accelerated to 70–90 per cent of the terminal speed of the slower wind (Fig. 8), and the gas is at a distance from the stars of order the stellar separation. Both of these conditions are satisfied by the 85 per cent cut-off attained via calibration of the dynamic model against hydrodynamic models. Interestingly, varying the value of the cut-off percentage has the effect of improving the fit to one spiral arm but reducing the quality of the fit to the other arm. Using the model A parameters (Table 2) the off-axis distance of the ballistic point from the line of centres, r_{max} , increases by a factor of ~ 3 between 70 and 90 per cent (Table 1), whereas the opening angle of the shock in-

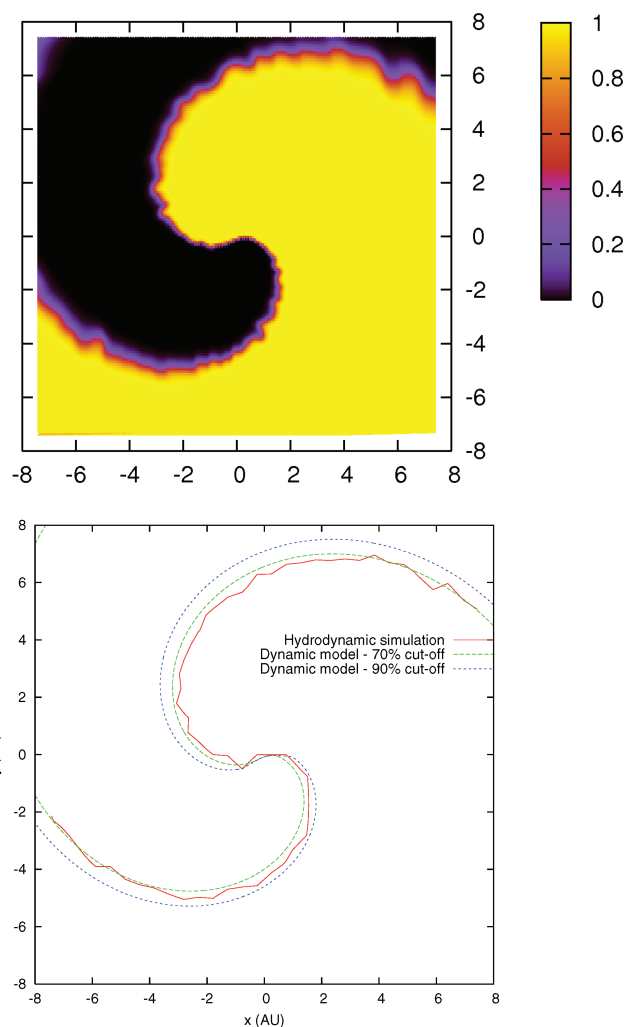


Figure 8. 3D plots viewed from above the orbital plane showing the position of the contact surface separating the stellar winds from a hydrodynamic simulation (top) and from the dynamical model with a varying cut-off percentage for the transition between the shock cap and the ballistic CD (bottom). The shading in the hydrodynamic simulation identifies the different stellar winds, where a value of 0.5 marks the CD. In these simulations an orbital period of 19.7 d, eccentricity, $e = 0.0$, stellar masses, $M_1 = M_2 = 30 M_\odot$, and terminal wind speeds of $v_{\infty 1} = v_{\infty 2} = 1500 \text{ km s}^{-1}$ were used. The mass-loss rate of the primary star was $\dot{M}_1 = 3 \times 10^{-7} M_\odot \text{ yr}^{-1}$ and that of the secondary star was $\dot{M}_2 = 1 \times 10^{-7} M_\odot \text{ yr}^{-1}$.

creases by roughly a half with a more linear relation. In Section 3.3 we show that there is little difference in the X-ray light curves when this percentage is varied slightly.

Fig. 9 shows the effect of the motion of the stars on the ballistic CD on scales of the order of the semimajor axis. The curvature of the CD close to the end of the shock cap is greatest when the relative orbital velocity of the stars is high. The smooth connection of the ballistic CD to the shock cap indicates that the assumptions inherent in the model are good at this level.

The structure of the ballistic CD at large scales is shown in Fig. 10 for a range of orbital eccentricities. At low orbital eccentricities, the spiral structures resemble the 3D hydrodynamical models of Walder & Folini (2000, 2002) and Lemaster, Stone & Gardiner (2007), the dust spiral models of the pinwheel nebula WR 104 by Harries et al. (2004) and Tuthill et al. (2008) and the CWo model for symbiotics developed by Kenny & Taylor (2007). Note, however, that this

Table 1. Transition points between the shock cap and the ballistic CD for varying percentages of the post-shock flow velocity. r_{\max} is calculated using equation (4). $\theta_{c1\infty}$ is the opening angle of the shock at the transition point measured from the primary star (see Fig. 3).

Cut-off (per cent)	r_{\max} (d_{sep})	$\theta_{c1\infty}$ ($^{\circ}$)
70	0.53	33
80	0.78	40
85	0.99	44
90	1.40	49

figure shows the projection of the CD on to the orbital plane, and not the position of the shocks either side of it. If the shocked region were largely adiabatic, the shocks would stand off from the CD and the width of the spiral structure on the orbital plane would be somewhat greater.

At $e = 0.9$ the secondary star moves very quickly through periastron, resulting in the projected CD (which encompasses the region of unshocked secondary wind) thinning to the left of the stars. In contrast, there exists a large region of unshocked secondary wind to the right of the stars, as the secondary star moves slowly around apastron. This creates a low-density cavity in the primary wind. The X-ray attenuation in such systems will depend on the orbital phase, as well as being sensitive to the position of the observer, and in principle may vary widely. For instance, in a system like η Car, the primary wind is very dense and much more strongly absorbing than

the secondary wind. An observer located on the positive x -axis at infinity will predominantly view through the low density unshocked wind of the secondary star, whereas an observer on the negative x -axis will predominantly view through the high-density unshocked wind of the primary star. As the column density scales directly with the density of the gas, these observers will see significantly different X-ray light curves. On the other hand, if the primary wind is more rarefied than the secondary wind, this behaviour reverses.

Finally, we note that in systems with highly eccentric orbits, the amount of attenuation at phases around apastron may depend on the skew angle of the shock cap which occurs around periastron. This is because the skew angle of the shock cap affects the duration and phase where primary/secondary wind material is emitted in a certain direction. Depending on the viewing angle into the system, the inclusion of aberration effects may result in a variation in the attenuation to emission concentrated near the apex of the shock cap due to the alteration in path-length through the more strongly absorbing wind.

3 AN EXAMPLE APPLICATION – X-RAY EMISSION AND ABSORPTION IN AN EARLY-TYPE BINARY

As an example application of the model described in Section 2, we consider the X-ray emission from hypothetical O+O and WR+O star colliding wind binaries. Model A is an O+O binary with an orbital period of 1 yr and semimajor axis $a = 4.3$ au. Model B

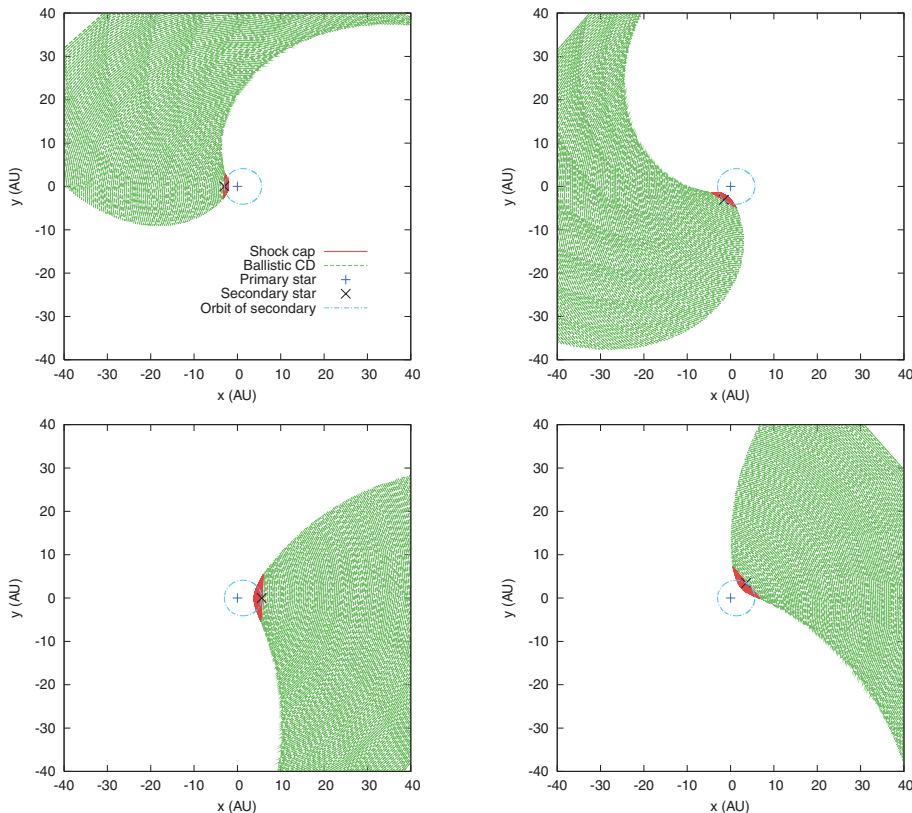


Figure 9. 3D plots viewed from above the orbital plane showing the position of the shock cap (red) and the structure of the ballistic CD (green) at various orbital phases from a simulation with $e = 0.3$ (see Table 2 for the other relevant parameters). The skew to the shock cap due to the orbital motion of the secondary star is included. From top left to bottom right: $\phi = 0.0, 0.1, 0.5$ and 0.7 . The curvature of the ballistic CD at $\phi = 0.0$ is caused by the high velocity of the secondary star around periastron passage. Note that the shocks either side of the CD are not displayed. The white area downstream of the ballistic CD in the corner of each plot is an artefact of the plotting software.

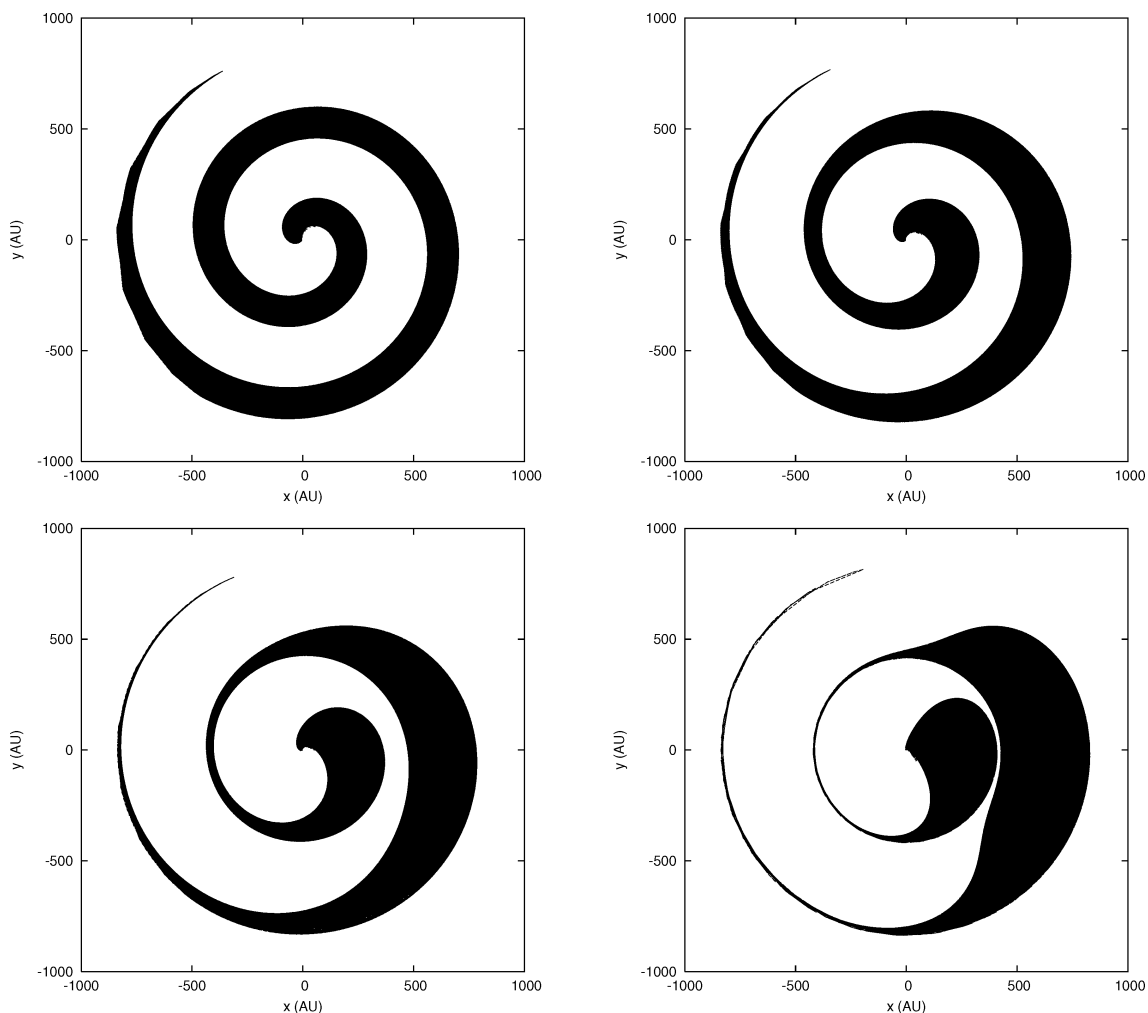


Figure 10. Plots of the large-scale structure of the ballistic CD in the orbital plane at $\phi = 0.0$ as a function of eccentricity. $e = 0.0, 0.3, 0.6$ and 0.9 from top left to bottom right, with the other parameters given in Table 2. The semimajor axis of the orbit is 4.30 au, and the orbital period is 1 yr. The black region on the plots shows the projection of the 3D CD on to the orbital plane, which encompasses the unshocked secondary wind. The white region mostly traces the unshocked primary wind. Note that the shocks either side of the CD are not displayed. The variation of the velocity and separation of the stars around the orbit increases with the orbital eccentricity, which results in the increasing asymmetry of the projected CD. The tapering of the black region at the tail of the spiral (most noticeable in the $e = 0.0$ and 0.3 plots) is due to the fact that the ballistic part is only traced back for two orbits and that the leading and trailing arms of the CD finish in different directions. Further details of the interaction at $e = 0.3$ are shown in Fig. 9.

examines the increasing effects of absorption as the orbital period is reduced to 1 month. The third model system (model C) consists of a WR star with a mass-loss rate of $2 \times 10^{-5} M_{\odot} \text{ yr}^{-1}$. The high velocities of the stellar winds are sufficient to cause the post-shock gas to emit at X-ray wavelengths, and both winds are essentially adiabatic in the systems considered (see Table 2). For the three models considered we use a distance of 1 kpc, interstellar medium (ISM) column of $5 \times 10^{21} \text{ cm}^{-2}$ and orbital eccentricity, $e = 0.3$.

3.1 The X-ray emission

The X-ray emission from the WCR is a function of the gas temperature and density. Since the dynamical model discussed in the previous section does not contain such information, we use a grid-based, 2D hydrodynamical calculation of an axis-symmetric WCR to obtain this. The numerical code is second-order accurate in time and space (Falle & Komissarov 1996; Falle, Komissarov

Table 2. Summary of the wind and orbital parameters of the model systems. η is the wind momentum ratio, and a the semimajor axis of the orbit. In each model the wind speeds and stellar radii adopted were $v_{\infty 1} = v_{\infty 2} = 2000 \text{ km s}^{-1}$ and $R_{*1} = R_{*2} = 10 R_{\odot}$. Cooling parameters are calculated for an orbital separation of $d_{\text{sep}} = a$. The half-opening angles, $\theta_{c1\infty}$, of the WCR are comparable to the 61° and 41° for models A and C, respectively, calculated using equation (3) of Eichler & Usov (1993).

Model	M_1 (M_{\odot})	M_2 (M_{\odot})	\dot{M}_1 ($M_{\odot} \text{ yr}^{-1}$)	\dot{M}_2 ($M_{\odot} \text{ yr}^{-1}$)	η	$\theta_{c1\infty}$ ($^{\circ}$)	P	a (au)	χ_1	χ_2
A	50	30	1.0×10^{-6}	2.0×10^{-7}	0.20	62.6	1 yr	4.3	100	500
B	50	30	1.0×10^{-6}	2.0×10^{-7}	0.20	62.6	1 month	0.81	20	100
C	50	50	2.0×10^{-5}	1.0×10^{-6}	0.05	41.0	1 yr	4.3	5	100

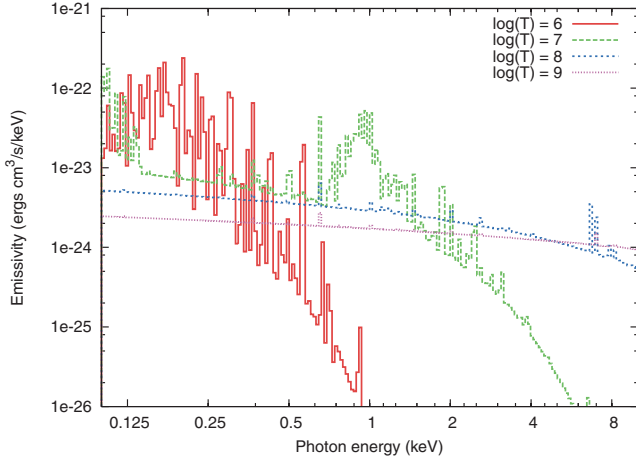


Figure 11. Emissivity of the solar abundance gas in the spectral energy range 0.1–10.0 keV at various temperatures (K) as calculated from the MEKAL thermal plasma code.

& Joarder 1998). The resulting emission as a function of off-axis distance is then mapped on to the coordinate positions in the 3D dynamical model. In this way we obtain the benefit of effectively modelling the thermodynamic and hydrodynamic behaviour responsible for the production of the X-ray emission, while simultaneously accounting for the effect of the motion of the stars on the large-scale structure of the WCR and the subsequent wind attenuation. Since the hydrodynamic calculation is 2D, the computational requirements remain low.

The X-ray emission calculated from each hydrodynamic cell in the WCR is $\Gamma(E) = n^2 V \Lambda(E, T)$, where n is the gas number density (cm^{-3}), V is the cell volume (cm^3) and $\Lambda(E, T)$ is the emissivity as a function of energy E and temperature T for optically thin gas in collisional ionization equilibrium ($\text{erg cm}^3 \text{s}^{-1}$). $\Lambda(E, T)$ is obtained from look-up tables calculated from the MEKAL plasma code (Leidahl, Osterheld & Goldstein 1995, and references therein) containing 200 logarithmically spaced energy bins in the range 0.1–10.0 keV, and 101 logarithmically spaced temperatures from 10^4 to 10^9 K. Solar abundances are assumed for the O star winds and the WR wind is assumed to have WN8 abundances (mass fractions of H/He = 0, C/He = 1.7×10^{-4} , N/He = 5×10^{-3} and O/He = 1×10^{-4}). The emissivity of solar abundance gas is shown in Fig. 11 and the corresponding opacity is shown in Fig. 12. The WN8 emissivities are very similar to those at solar abundance. Opacity values are also similar for solar and WN8 abundances, with the most significant difference being a factor of 2 increase at 10^4 K at energies below ~ 1 keV.

The emission values are then appropriately scaled for the changing stellar separation around the orbit ($L_x \propto d_{\text{sep}}^{-1}$ in the adiabatic limit; Stevens et al. 1992) and placed on to the 3D shock cap and ballistic CD. Emission values are assigned to points within $3 d_{\text{sep}}$ of the apex of the WCR. This accounts for ~ 90 per cent of the 0.1–10 keV emission and >99 per cent of the 2–10 keV emission.

3.2 The attenuation

To compute X-ray light curves, the orientation of the observer relative to the system must be specified. Since the model assumes the orbit of the stars is in the xy plane, viewing angles into the system can be described by the inclination angle that the line-of-sight makes with the z -axis, i and the angle the projected line-of-sight

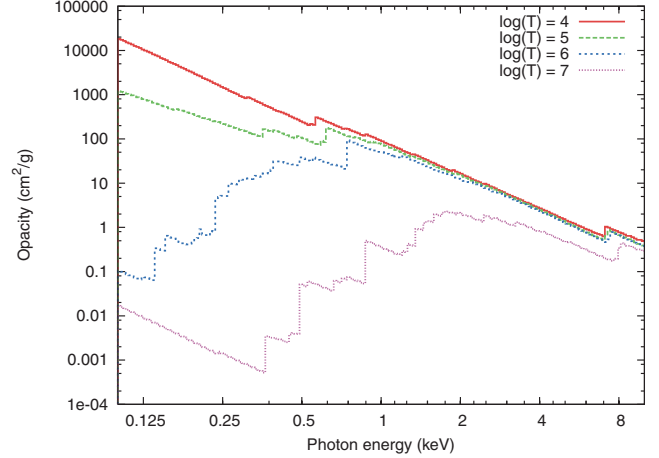


Figure 12. Opacity (g cm^{-2}) in the spectral energy range 0.1–10.0 keV at various temperatures (K).

makes with the major axis of the orbit, θ . Positive values of θ correspond to projected lines-of-sight in the prograde direction from the positive x -axis. The components of the unit vector along the line-of-sight, \hat{u} , are thus

$$u_x = \cos \theta \sin i,$$

$$u_y = \sin \theta \sin i,$$

$$u_z = \cos i.$$

There are three ways in which the intrinsic X-ray emission can be attenuated. First, it can be occulted by the stars (this effect, of course, is greatest in short period systems). Second, there will be some absorption through the unshocked stellar winds. Finally, there will be attenuation through the shocked gas in the WCR. The latter is only important in systems where the shocked gas of at least one of the winds is strongly radiative, otherwise the gas in the WCR remains hot and the attenuation through it is small. However, if there is significant cooling, as for example occurs when the cool wind in symbiotic systems is shocked, a thin, dense and cold layer of gas is formed at the CD, which will be a significant source of attenuation in the system. Significant cooling of the WCR can also occur in early-type binary systems of which η Car is an example. We now describe how attenuation by each of the above-mentioned methods is calculated in our model.

3.2.1 Occultation by the stars

An important line-of-sight effect in binary star systems is occultation, particularly in the case of eclipsing binaries. To calculate this effect in our model, a line-of-sight is traced from each emitting region on the shock cap and ballistic CD, and its distance of closest approach to the centre of each star is calculated. If this distance is less than the radius of the star, and the star is in front of the emitting region, then occultation occurs, and none of the emission from the emitting region being considered reaches the observer.

A visual representation of the occultation of the WCR by the primary star is shown in Fig. 13. The degree of occultation can be reduced by reducing the inclination angle i (since the strongest X-ray emission occurs at the apex of the WCR). Although not shown, the phase at which the maximum occultation occurs can be altered by changing the value of θ .

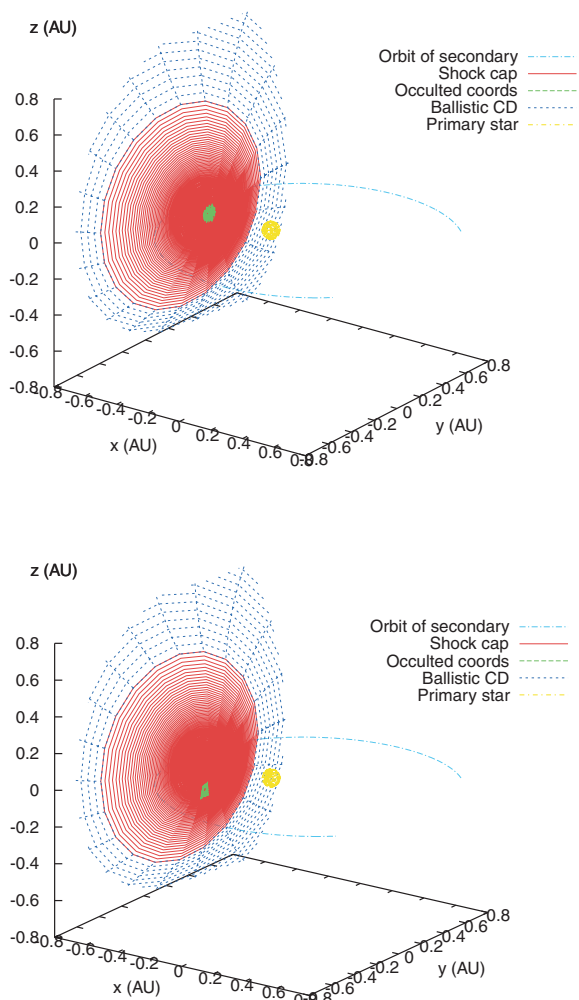


Figure 13. 3D plots showing occultation effects for two different viewing angles at periastron ($\phi = 0.0$) with $e = 0.3$ and an orbital period $P = 1$ month. The occulted emission from the shock cap is represented in green (this is essentially the ‘shadow’ of the occulting star – the secondary star is hidden behind the shock cap). The top panel shows the case where $i = 90^\circ$ and $\theta = 0^\circ$. The primary star is directly in front of the secondary star and the apex of the WCR is occulted. In the bottom panel $i = 70^\circ$ and $\theta = 0^\circ$. The line-of-sight peers over the top of the primary star and the ‘shadow’ moves below the apex of the WCR – less emission is occulted as a result. The finite number of coordinates on the shock cap, together with the trapezium-shaped emission regions, account for the particular shape of the ‘shadow’ in this case. Aberration of the WCR is included in both plots.

Occultation causes little change to the observed luminosity over the entire orbit for the model A system. This is due to the relatively small size of the stars in comparison to the extended emitting region for the 0.1–10.0 keV X-rays. Occultation effects become more noticeable in shorter period systems, and/or those with highly eccentric orbits (since the linear size of the shock cap is $\propto 1/d_{\text{sep}}$). Occultation is also favoured where one (or both) of the stars has a large stellar radius (e.g. η Car; Parkin et al., in preparation), and when i is large. For instance, the $e = 0.9$ light curve in Fig. 14 shows a pronounced occultation effect at orbital phase $\phi \simeq 1.00$, during which the emission falls sharply by a factor of 2. The width of the minimum due to occultation effects is very narrow as the high eccentricity means that the stars move rapidly through periastron, but the depth of the minimum is large (~ 75 per cent of the intrinsic 2–10 keV emission is occulted).

3.2.2 Absorption by the unshocked stellar winds

For inclinations, $|i| \geq \pi/2 - \theta_{c1\infty}$, the line-of-sight from emitting regions near the apex of the WCR will intersect the CD numerous times as it spirals out, and thus traverses first through one wind and then the other etc. The total column density along a line-of-sight is then the sum of the individual column densities along the specific distances travelled in each wind. Accurate knowledge of where the line-of-sight intersects the CD, and the density of the gas at any point in space is therefore required if the total column density along a given sightline is to be calculated.

To determine if and where an intersection through the CD occurs, the shock cap and ballistic CD are tessellated into a sequence of triangular planar facets constructed between three neighbouring coordinates (\mathbf{P}_a , \mathbf{P}_b and \mathbf{P}_c). To determine if the line-of-sight intersects a given triangle the normal to the plane in which the triangle lies, $\hat{\mathbf{n}}$, is calculated from

$$\hat{\mathbf{n}} = (\mathbf{P}_b - \mathbf{P}_a) \times (\mathbf{P}_c - \mathbf{P}_a). \quad (7)$$

The dot product of $\hat{\mathbf{n}}$ with the line-of-sight vector gives the angle between the line-of-sight and the plane. If the resultant angle is non-zero the line-of-sight vector will intersect the plane in which the triangular facet lies at some point in space.

The component vectors to the intersection point (x_{int} , y_{int} and z_{int}) are found by substituting the line parameter at the intersection point,

$$\kappa = \frac{n_x x_{\text{cap}} + n_y y_{\text{cap}} + n_z z_{\text{cap}} + n_{\text{const}}}{n_x u_x + n_y u_y + n_z u_z}, \quad (8)$$

into the equations

$$x_{\text{int}} = x_{\text{cap}} + \kappa u_x,$$

$$y_{\text{int}} = y_{\text{cap}} + \kappa u_y,$$

$$z_{\text{int}} = z_{\text{cap}} + \kappa u_z,$$

where the equation of the plane with normal $\hat{\mathbf{n}}$ and vector components n_x , n_y and n_z is

$$n_x x + n_y y + n_z z + n_{\text{const}} = 0. \quad (9)$$

In general, the intersection occurs outside of the triangular facet. Unit vectors are constructed between the corner points of the facet and the intersection point to determine whether the intersection occurs within its boundaries. The three dot products between these three unit vectors gives the angles θ_a , θ_b and θ_c . Only if the intersection point lies within the boundaries of the triangular facet will the equation $\theta_a + \theta_b + \theta_c = 2\pi$ be satisfied (see Fig. 15). By looping over the entire sequence of triangles, every possible intersection of the line-of-sight with the CD is determined.

With the coordinates of the intersection points (x_{int} , y_{int} and z_{int}), it is a simple task to calculate the column density through the unshocked winds, σ_w . Lines-of-sight which pass very close to the stars sample the acceleration region of the wind. Therefore, we use a β -velocity law of the form

$$v(r) = v_\infty \left(1 - \frac{R_*}{r}\right)^\beta \quad (10)$$

to determine the density of the wind at radius r from the star. β describes the acceleration of the wind with $\beta = 0.8$ appropriate for O star winds (Lamers & Cassinelli 1999). Because the width of the WCR is not considered in our model, the volume of unshocked wind and the resulting attenuation are overestimated, though this approximation will not have a significant impact on our results.

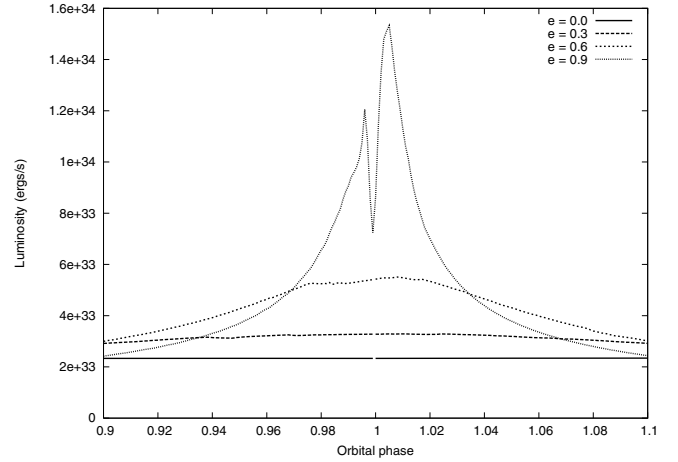
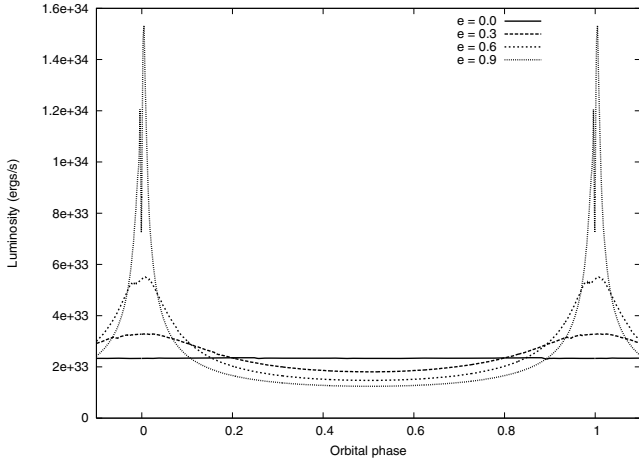


Figure 14. 0.1–10.0 keV light curves for model B with $e = 0.0, 0.3, 0.6$ and 0.9 with occultation included. Left: the variability shown over an entire orbital period. Right: the variation over the orbital phase range 0.9–1.1. Occultation is highest at periastron for the $e = 0.9$ light curve because the size of the shock cap relative to the primary star is smallest at this time. Orbital motion induced skew causes the pre-minimum intrinsic luminosity to be lower than the post-minimum, this effect increases with orbital eccentricity. For all curves $i = 90^\circ$ and $\theta = 0^\circ$. Interstellar absorption has not been considered in these calculations.

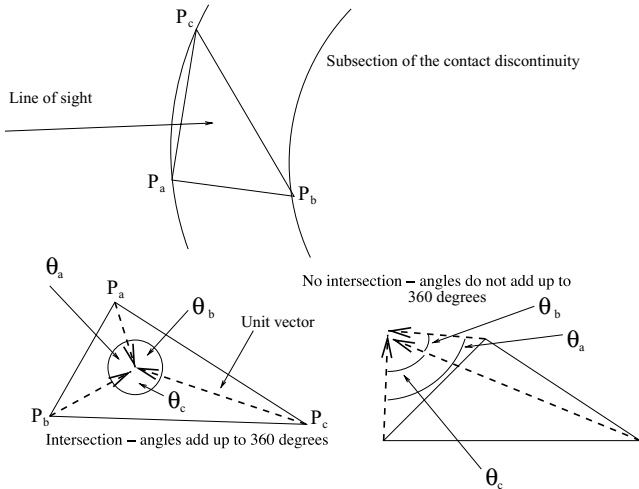


Figure 15. The method used to determine whether a given line-of-sight intersects the CD through a specific triangular facet. Triangles are constructed over the entire shock cap and ballistic CD from adjacent coordinates and the unit vectors between the corners of the triangle and the intersection coordinate are used to determine if the intersection occurs within the boundary of the triangle.

3.2.3 Absorption by the shocked stellar winds

As already mentioned, the attenuation of X-rays through the shocked wind(s) needs to be considered if one or both winds strongly cool. In the O+O and WR+O star binaries considered in this section, the shocked gas is largely adiabatic. However, for completeness, we discuss here a methodology for calculating the absorption due to X-rays intersecting a cold dense layer of post-shock gas at the CD. This is applied to models of η Car in Parkin et al. (in preparation). In Figs 18–24 this effect does not need to be considered.

The surface density, σ_s , of the post-shock gas along the CD, when both winds have $\chi \lesssim 1$, has been computed by Girard & Willson (1987), Canto et al. (1996) and Kenny & Taylor (2005). In each of these works, turbulence in the post-shock flow is assumed to fully mix the material from both winds and the surface density

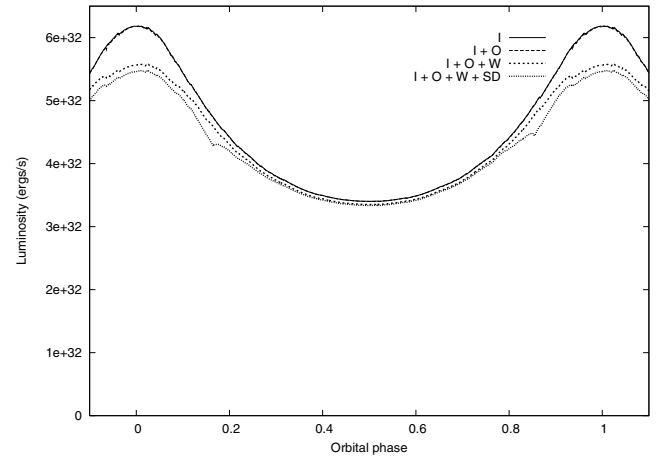


Figure 16. The effect of the various attenuation mechanisms on the observed 0.1–10.0 keV emission as a function of orbital phase for model A. The unattenuated intrinsic emission (I), intrinsic emission with occultation (I+O), intrinsic emission with occultation and wind attenuation (I+O+W) and intrinsic emission with occultation, wind attenuation and attenuation due to intersection of the shocked gas (I+O+W+SD) are shown. Attenuation through the shocked gas (SD) is only important if the shocked gas can cool efficiently and is shown here purely for illustration of its effect. The assumed viewing angles are $i = 90^\circ$ and $\theta = 0^\circ$, and the other model parameters are listed in Table 2. The skew in the WCR due to orbital motion is included. Equation (30) of Canto et al. (1996) has been used to calculate surface densities as this provides an approximate upper limit to the attenuation by shocked gas. Interstellar absorption ($\sim 5 \times 10^{21} \text{ cm}^{-2}$) is included. The variation in the intrinsic emission is proportional to $1/d_{\text{sep}}$.

calculated is for shocked gas from both winds. Alternatively, if only one of the winds is radiative (i.e. the other remains largely adiabatic), or the post-shock flow is assumed not to mix, then the surface density can be calculated from considering conservation of mass flux (e.g. Antokhin, Owocki & Brown 2004). To calculate the surface densities in Figs 16 and 17 we have used equation (30) of Canto et al. (1996).

In our model, the ballistic part of the WCR is asymmetric due to orbital motion. Since the pre-shock flow is practically tangential to the CD at this point, we calculate the total surface density of the

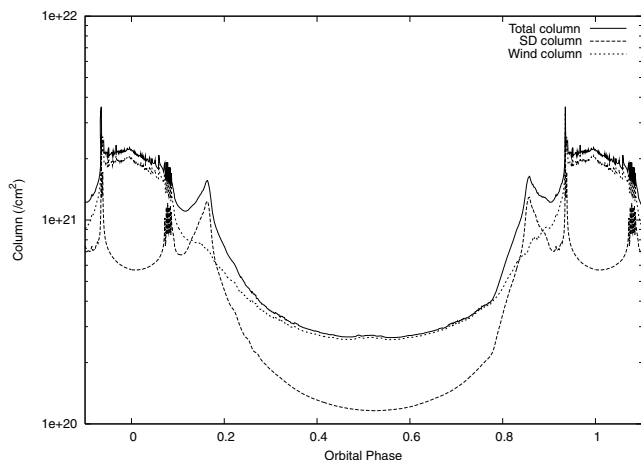


Figure 17. Variation of emission weighted column density as a function of orbital phase. Interstellar absorption is not included.

post-shock winds (which in this subsection are assumed to cool) in this region by considering conservation of mass flux. The surface density of the post-shock gas close to the apex of the WCR varies by over an order of magnitude between periastron and apastron when $e = 0.9$.

Since the width of the cool dense layer of gas alongside the CD is not infinitely thin, the degree of absorption through it depends on the angle subtended between the line-of-sight and the normal to its (i.e. the CD's) surface, γ . The column density intersected by the line-of-sight is therefore

$$\sigma'_s = \frac{\sigma_s}{\cos \gamma}, \quad (11)$$

where σ_s is the actual surface density of the cooled layer. When the line-of-sight becomes closely tangential to the CD, σ'_s can become large, even if σ_s itself is not particularly large.

The maximum value of σ'_s is constrained by the curvature of the WCR and the finite path-length through the shocked gas. To determine the maximum path-length requires knowledge of the width of the cooled layer and its radius of curvature at the point of interest on the CD. On the shock cap the density of the cooled post-shock region, ρ_{ps} , can be determined by equating the ram pressure of the pre-shock gas with the thermal pressure of the post-shock gas (Kashi & Soker 2007):

$$\rho_{ps} = \frac{m_H \rho_1(r) (v_{\infty 1} \sin \xi)^2}{k_B T_{ps}}, \quad (12)$$

where T_{ps} is the temperature of the cooled post-shock gas (T_{ps} is taken to be 10^4 K), $\rho(r)$ is the pre-shock gas density as a function of distance from the respective star, ξ is the angle between the pre-shock velocity vector and the tangent to the shock surface and m_H and k_B are the mass of a hydrogen nucleus and Boltzmann's constant, respectively. The thickness of the cooled layer, l_{shock} , is then

$$l_{shock} = \frac{\sigma_s}{\rho_{ps}}. \quad (13)$$

The thickness of the cooled layer in the ballistic CD region cannot be calculated in this manner because the shocks are now fully oblique. Therefore, a linear extrapolation is used to determine the downstream thickness.

The radius of curvature at a point on the shock cap is

$$\Lambda = \left| \frac{ds}{d\hat{t}} \right|, \quad (14)$$

where ds is the distance between two points on the WCR and $d\hat{t}$ is the difference in the unit vectors tangent to the WCR at those two points. Consideration of the maximum path-length through the cool dense layer, d_{max} , then gives the maximum value for σ'_s/σ_s as

$$\left| \frac{\sigma'_s}{\sigma_s} \right|_{max} \simeq \frac{d_{max}}{l_{shock}} = \sqrt{4 + \frac{8\Lambda}{l_{shock}}}. \quad (15)$$

The skewing of the shock cap due to orbital motion will evoke an asymmetry in the post-shock gas density (Lemaster et al. 2007). This is naturally accounted for in equations (12) and (15).

3.2.4 The observed emission

In the hypothetical binary systems considered in this paper, the shocked gas in the WCR remains hot as it flows out of the system and thus contributes insignificantly to the absorption. Hence the total column density along a given line-of-sight is the sum of the column densities through the unshocked winds. The attenuation declines as the line-of-sight leaves the system, and is negligible at the distances which our model extends to (the distance the wind flows over two orbits).

Absorption cross-sections for solar abundance gas at 10^4 K are used to obtain the optical depth, τ , along specific lines-of-sight in 200 logarithmically spaced bins over the energy range 0.1–10.0 keV. The observed attenuated emission, $I_{obs} = I_0 e^{-\tau}$, where I_0 is the intrinsic emission.

Fig. 16 demonstrates the effect of including the various attenuation mechanisms on the resultant emission. As previously mentioned, occultation causes little reduction in emission because of the minute size of the stars compared to the extended WCR (Fig. 13). For the assumed position of the observer, absorption by the unshocked winds increases as the stars approach each other and reaches a maximum at periastron. For illustrative purposes we also show the attenuation that occurs if the post-shock gas cools and forms a thin dense layer along the CD (this does not occur in the systems considered since the shocked gas remains largely adiabatic as it flows out of the system). When the line-of-sight becomes closely tangential to the WCR the path-length of X-rays through the shocked gas and the subsequent attenuation via this mechanism reaches a maximum. This can be seen in the small dips in the light curve at orbital phases 0.18 and 0.82, with corresponding peaks in the emission-weighted column shown in Fig. 17. The emission weighted column density is calculated as $\sum \sigma_{tot} I_0 / \sum I_0$, where the summation is over all sightlines to emitting regions and σ_{tot} is the total column density (cm^{-2}) along each sightline. This weighting is more informative than the column densities presented in Lemaster et al. (2007) which were only calculated along a single sightline into the system.

Resolution tests have determined that the minimum number of phase steps required for convergence of the attenuated X-ray light curves is dependant on the ratio v_{orb}/v_{sl} , with of order 1000 phase steps required for an orbit with $e = 0.9$ and $v_{orb}/v_{sl} \approx 1$.

3.3 Results

3.3.1 The X-ray light curve

In this section we compute X-ray light curves for the hypothetical systems considered. For the O+O systems we use emissivity and opacity data calculated assuming solar abundances (Figs 11 and 12, respectively). For the WR wind we use data appropriate for WN 8 abundances.

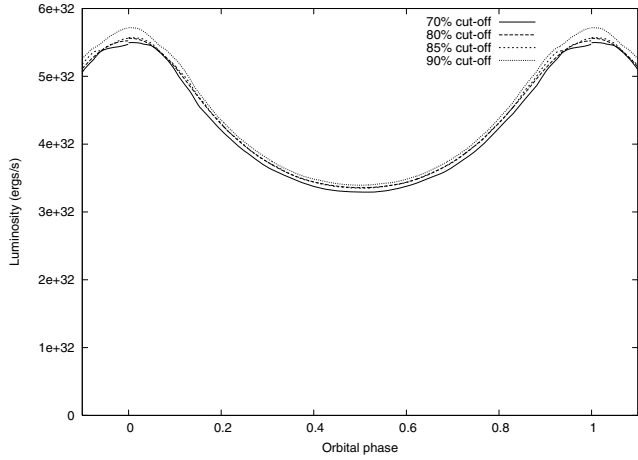


Figure 18. Synthetic 0.1–10.0 keV light curves for different transition positions between the shock cap and the point where the flow in the WCR is assumed to behave ballistically for model A (period of 1 yr, semimajor axis of 4.3 au). The transition point is specified in terms of a percentage of the terminal speed of the slower of the two winds, v_{sl} . The assumed line-of-sight is $i = 90^\circ$ and $\theta = 0^\circ$. Interstellar absorption is included.

Fig. 18 shows the synthetic light curves produced for models where the transition between the shock cap and the ballistic CD is varied. There is a maximum divergence of ~ 6 per cent between cases where the transition occurs at a velocity cut-off of 70 and 90 per cent of the speed of the slower wind, which shows that the resulting light curves are not very sensitive to this assumption.

Varying the orbital inclination angle changes the amount of attenuation that the intrinsic emission suffers on its way to the observer. However, there is little circumstellar attenuation for model A (Fig. 19, left-hand panel), and the synthetic light curves are almost identical over the entire orbital period. This is because the emitting volume is large (so occultation by the stars is negligible), and because the stellar separation is wide, so that the circumstellar density at the WCR is relatively low. Attenuation effects become more prominent if the orbital period is reduced to 1 month (Fig. 19, right-hand panel), and distinct differences in the light curves occur around periastron. The $i = 0^\circ$ light curve is smooth, and reflects the fact that the increase in the intrinsic emission due to the changing orbital separation ($L_x \propto 1/d_{sep}$) more than offsets the peak in attenuation

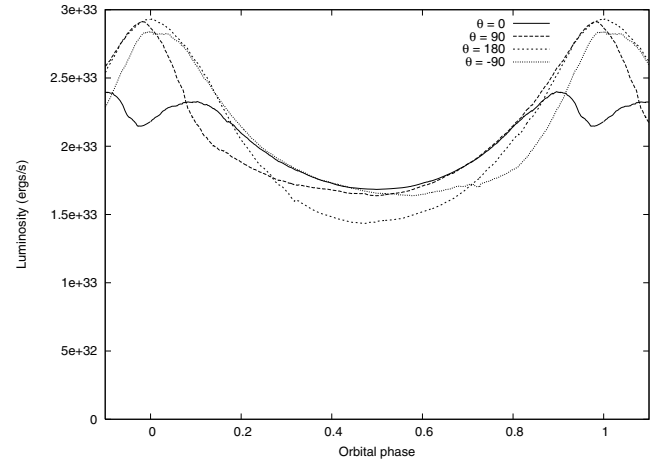
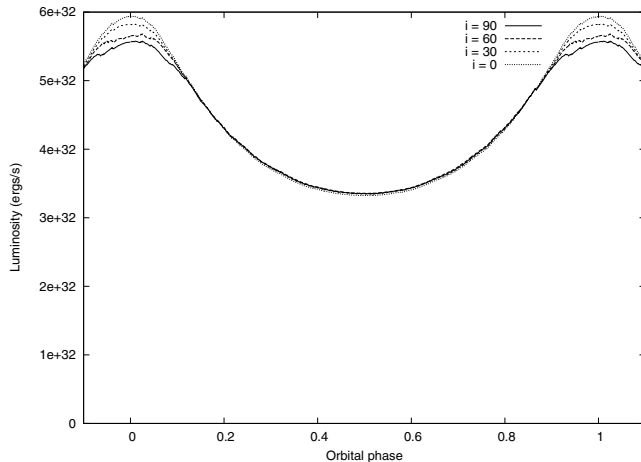


Figure 20. Synthetic 0.1–10.0 keV emission light curves for model B (see Table 2) with $i = 90^\circ$ and various line-of-sight angles, θ . The observed emission is clearly sensitive to the viewing angle. Interstellar absorption is included.

through the primary wind at periastron. Increasing the inclination enhances the attenuation around periastron. The dip seen in both the $i = 60^\circ$ and 90° curves is offset from the time of periastron ($\phi = 1.0$) because of the skew to the WCR caused by orbital motion. As already mentioned in Section 3.2.1, the stars fail to provide any significant eclipse of the emitting region.

Fig. 20 examines the dependence of the observed emission on the angle subtended between the line-of-sight and the semimajor axis. The $\theta = 90^\circ$ and -90° curves appear to be almost identical reflected copies around orbital phase $\phi \simeq 0.5$, with the differences around periastron being due to the aberration of the WCR. Absorption does not strongly affect the observed emission (even if the orbital period is reduced to 1 month) as the density contrast between the O star winds is not very large. The largest difference between the model results (~ 25 per cent) occurs at periastron. A comparison between current observational data and such models may allow constraints to be placed on the orientation of specific O+O star systems.

The higher primary mass-loss rate in the WR+O system leads to a greater dependence of the observed emission on the line-of-sight (Figs 21 and 22), as well as higher X-ray luminosities. The minimums in the curves close to periastron in Fig. 21, especially

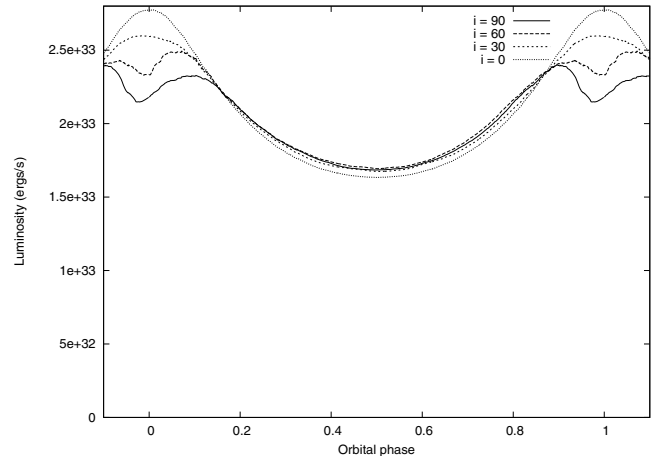


Figure 19. Synthetic 0.1–10.0 keV emission light curves for various inclination angles, i , for model A (left, $a = 4.3$ au) and model B (right, $a = 0.81$ au). Model parameters are indicated in Table 2. Interstellar absorption is included.

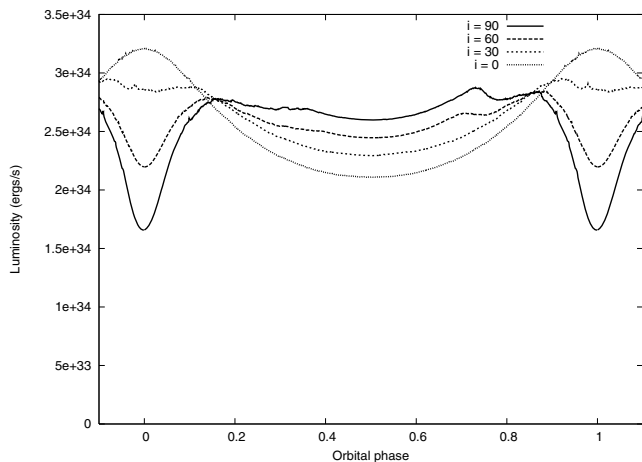


Figure 21. Synthetic 0.1–10.0 keV emission light curves for model C (see Table 2) with various inclination angles, i . Interstellar absorption is included.

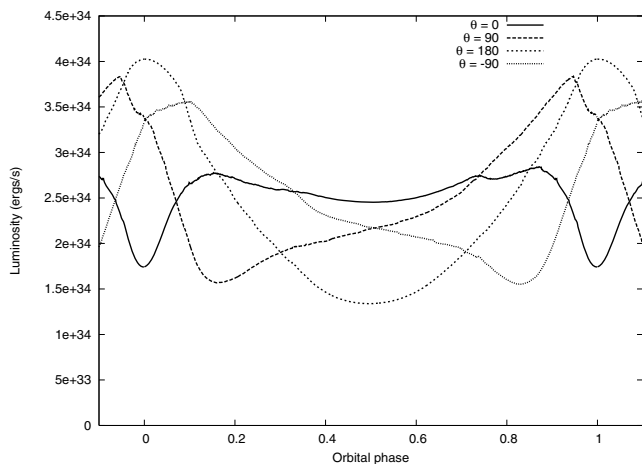


Figure 22. Synthetic 0.1–10.0 keV emission light curve for model C (see Table 2) with inclination $i = 90^\circ$ and various line-of-sight angles, θ . Interstellar absorption is included.

in the case of the $i = 90^\circ$ curve, are the result of the X-rays passing through the dense WR wind. However, there is again little difference between the $i = 60^\circ$ and 90° curves at apastron as the WCR is viewed predominantly through the less dense O star wind, though the attenuation at lower inclinations is slightly higher as the apex of the WCR is viewed through the denser wind from the WR star. Rotating the line-of-sight within the orbital plane again causes significant alterations to the observed emission (Fig. 22). The $\theta = 0^\circ$ curve sees the largest degree of attenuation around periastron and the lowest around apastron, with the opposite being true for the $\theta = 180^\circ$ curve. As was also the case in Fig. 20, the $\theta = 90^\circ$ and -90° light curves appear to be almost perfect reflected copies of each other. The dip seen in the $\theta = 90^\circ$ curve at orbital phase $\phi \simeq 0.17$ marks opposition. Features such as these could be particularly useful for constraining the orientation of systems.

Fig. 23 shows the variation with phase of the emission weighted column density for the three hypothetical systems considered. The column density is highest when viewed through the primary wind, and lowest when viewing through the secondary wind. It is lowest for model A, and is approximately five times higher when the period is reduced to 1 month (model B). This simply reflects the \simeq five

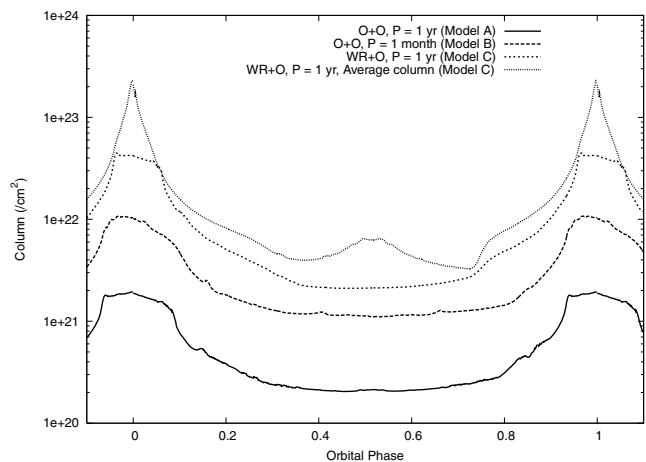


Figure 23. Variation of the emission weighted column density as a function of orbital phase for the O+O and WR+O star systems considered. The average column is also shown for the WR+O star system to demonstrate the difference between this and an emission-weighted column. Interstellar absorption is included.

times smaller separation and the $\simeq 30$ times higher densities. The ~ 10 times changes in the column density between apastron and periastron in model A curve reflects the 1.86 times change in stellar separation and five times change in wind density (or stellar mass-loss rate) as the line-of-sight switches from the secondary wind into the primary wind.

The different slopes of the column density either side of periastron are caused by the asymmetry of the WCR. The rise in column density at $\phi \sim 0.8$ begins when the shock cap rotates and lines-of-sight start to see the emission through the denser primary wind. The rise occurs at an earlier phase for the WR+O system because of the lower value of the wind momentum ratio and the narrowing of the opening angle of the WCR. At $\phi = 0.964$ and 0.055 the slope in the emission weighted column is reduced, and this feature marks the point where the bow shock arms are tangential with the line-of-sight. When the emission weighted column density is plotted alongside the average column density the change in slope occurs at a point where the two curves intersect. The average column density has a continual rise and a peak at periastron. This tells us that the column density to the entire emission region reaches a maximum at periastron, whereas attenuation to the points with highest intrinsic emission remains roughly constant for a short period. It is also interesting that both the O+O and WR+O systems with $P = 1$ yr (models A and C, respectively) have flatter profiles at maximum column density. This indicates that the shape of the column density curve is sensitive to the aberration and orbital-induced curvature of the WCR, and thus to the orbital period.

3.3.2 X-ray spectra

Fig. 24 shows synthetic spectra at periastron and apastron for the simulations performed. The slope of the spectra at high energies is the same for the O+O systems since the pre-shock velocities, and therefore post-shock gas temperatures, do not change. In all cases spectra at apastron show lower flux in the 2.0–10.0 keV energy band, although flux below 1 keV is higher. This is because the intrinsic emission scales as $1/d_{\text{sep}}$, but this is weaker when viewed through the companion's wind. The low energy turnover in the periastron

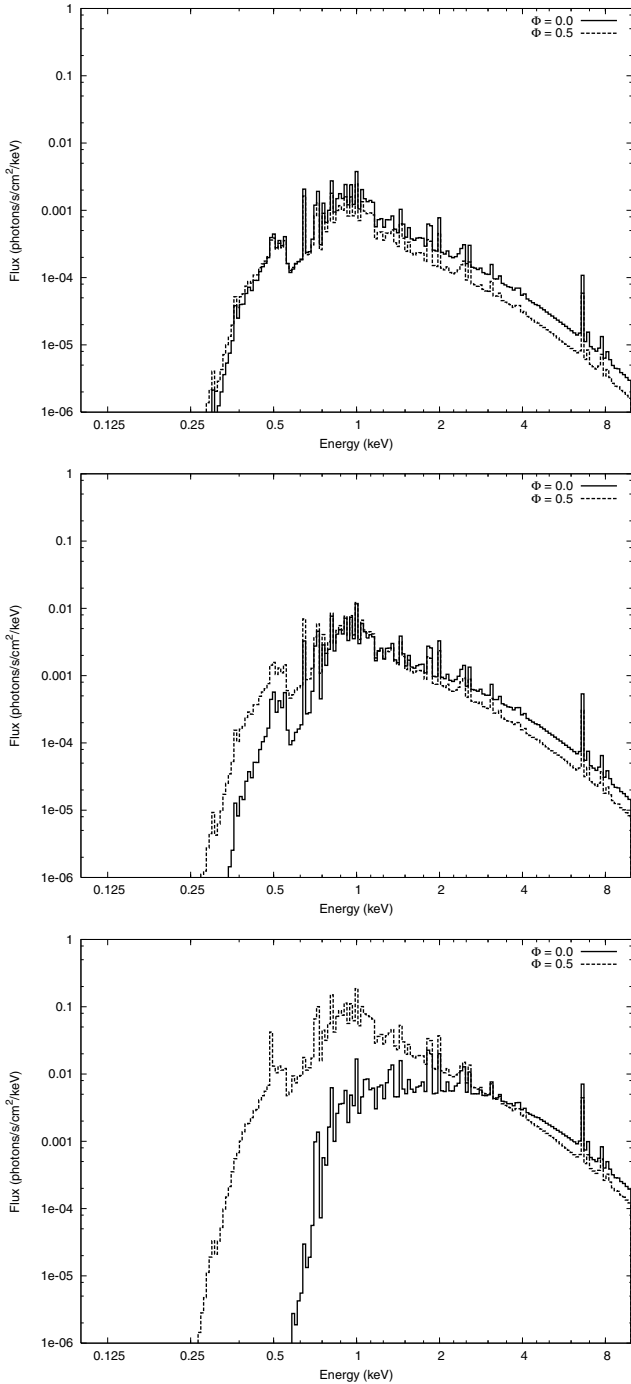


Figure 24. Synthetic 0.1–10.0 keV spectra at periastron and apastron for model A (top), B (middle) and C (bottom). The viewing angles are $i = 90^\circ$ and $\theta = 0^\circ$. Interstellar absorption is included. The corresponding light curves for these spectra are shown in Figs 19, 20 and 21.

spectrum extends to higher energies for the WR+O system due to the higher mass-loss rate and absorption of the WR wind.

4 CONCLUSIONS

We have presented a 3D dynamical model of the colliding winds in binary systems where both stars drive a significant wind. In circular systems, the WCR adopts a spiral shaped structure similar to those observed in massive binary star systems. In systems with eccentric

orbits, the shape of the WCR becomes increasingly deformed as the eccentricity increases, with the winds increasingly being channelled into a specific direction. A major advantage of the model is its low computational cost and the fact that it can be easily adapted to model a wide variety of observational data (from the radio to γ -ray) and systems (from early-type binaries, to γ -ray binaries with a pulsar wind, to symbiotic novae).

As an example exercise, the X-ray emission from hypothetical O+O and WR+O star systems was modelled. The intrinsic emission was computed from a 2D grid-based hydrodynamical model of the WCR, and then mapped on to the surface separating the winds in the 3D dynamical model. Absorption due to the unshocked stellar winds (and also cooled post-shock material) can be considered, although in the hypothetical systems that were modelled the gas in the WCR remains largely adiabatic as it flows out of the system so that only the former is calculated. Ray tracing through the 3D spiral structures then gives the attenuated emission, and synthetic spectra and light curves are produced.

The light curves and spectra show that observational characteristics of the X-ray emission from early-type binaries can be reproduced. For instance, the model with a 1-yr orbit (model A) is representative of wide O+O binaries such as HD 15558 (De Becker et al. 2006a), and in this particular system could be useful in determining whether there are two or three counterparts. The results from the 1 month orbit simulation (model B) are instead most applicable to X-ray observations of close O+O binaries such as ι Orionis (Pittard et al. 2000), CygOB2#8A (De Becker et al. 2006b) and HD 93403 (Rauw et al. 2000), to name but a few. The model can also tackle systems with different abundances for each wind such as WR+O star systems. Our WR+O star model with a 1 yr orbital period (model C) is applicable to systems like WR 25, WR 108, WR 133, WR 138 (van der Hucht 2001), and among the WN stars and WR 19, WR 125, WR 137, WR 98a, WR 104 and WR 140 (Pollock et al. 2005; Pittard & Dougherty 2006) among the WC stars.

Mass-loss rate determinations can be made from comparison of the predicted magnitude of the X-ray flux with observations (Stevens 1996; Pittard & Corcoran 2002). In principle it is possible to use the shape of the X-ray light curve to constrain the inclination and orientation of the system. Our results reveal that for wind momentum ratios of order 0.2, the lack of significant absorption means that this will be very difficult if applied to O+O star systems with periods of order 1 yr, but becomes possible for orbital periods of order 1 month. The variation in absorption is much more significant when the wind momentum ratio is lower and the density of the winds is more disparate. This is the case for WR+O, LBV+O and LBV+WR systems.

In future work we will apply the dynamical model to the X-ray and forbidden line emission from η Car, the X-ray light curve of WR 140 and emission line profiles of colliding wind binaries.

ACKNOWLEDGMENTS

We would like to thank Perry Williams for the 2D code which was the basis for the 3D model in this work. ERP thanks the University of Leeds for funding. JMP gratefully acknowledges funding from the Royal Society.

REFERENCES

- Aharonian F. et al., 2005a, A&A, 442, 1
- Aharonian F. et al., 2005b, Sci, 309, 746

- Albert J. et al., 2006, *Sci*, 312, 1771
- Antokhin I. I., Owocki S. P., Brown J. C., 2004, *ApJ*, 611, 434
- Bisikalo D. V., Boyarchuk A. A., Kilpio E. Yu., Tomov N. A., Tomova M. T., 2006, *Astron. Rep.*, 50, 722
- Bogovalov S. V., Khangulyan D., Koldoba A. V., Ustyugova G. V., Aharonian F. A., 2008, *MNRAS*, 387, 63
- Canto J., Raga A. C., Wilkin F. P., 1996, *ApJ*, 469, 729
- Contreras M. E., Montes G., Wilkin F. P., 2004, *Rev. Mex. Astron. Astrofis.*, 40, 53
- De Becker M., Rauw G., Manfroid J., Eenens P., 2006a, *A&A*, 456, 1121
- De Becker M., Rauw G., Sana H., Pollock A. M. T., Pittard J. M., Blomme R., Stevens I. R., van Loo S., 2006b, *MNRAS*, 371, 1280
- Dougherty S. M., Williams P. M., Pollacco D. L., 2000, *MNRAS*, 316, 143
- Dougherty S. M., Beasley A. J., Claussen M. J., Zauderer B. A., Bolingbroke N. J., 2005, *ApJ*, 623, 477
- Dubus G., Cerutti B., Henri G., 2008, *A&A*, 477, 691
- Eichler D., Usov V., 1993, *ApJ*, 402, 271
- Falle S. A. E. G., Komissarov S. S., 1996, *MNRAS*, 278, 586
- Falle S. A. E. G., Komissarov S. S., Joarder P., 1998, *MNRAS*, 297, 265
- Foellmi C. et al., 2008, *Rev. Mex. Astron. Astrofis.*, 44, 3
- Gawryszczak A. J., Mikolajewska J., Rozyczka M., 2002, *A&A*, 385, 205
- Gayley K. G., Owocki S. P., Cranmer S. R., 1997, *ApJ*, 475, 786
- Girard T., Willson L. A., 1987, *A&A*, 183, 247
- Harries T. J., Monnier J. D., Symington N. H., Kurosawa R., 2004, *MNRAS*, 350, 565
- He J. H., 2007, *A&A*, 467, 1081
- Henley D. B., Corcoran M. F., Pittard J. M., Stevens I. R., Hamaguchi K., Gull T. R., 2008, *ApJ*, 680, 705
- Johnston S., Ball L., Wang N., Manchester R. N., 2005, *MNRAS*, 358, 1069
- Kashi A., Soker N., 2007, *MNRAS*, 378, 1609
- Kenny H. T., Taylor A. R., 2005, *ApJ*, 619, 527
- Kenny H. T., Taylor A. R., 2007, *ApJ*, 662, 1231
- Khangulyan D., Hnatic S., Aharonian F., Bogovalov S., 2007, *MNRAS*, 380, 320
- Khangulyan D., Aharonian F., Bosch-Ramon V., 2008, *MNRAS*, 383, 467
- Lamers H. J. G. L. M., Cassinelli J. P., 1999, *Introduction to Stellar Winds*. Cambridge Univ. Press, Cambridge
- Leidahl D. A., Osterheld A. L., Goldstein W. H., 1995, *ApJ*, 438, L115
- Lemaster M. N., Stone J. M., Gardiner T. A., 2007, *ApJ*, 662, 582
- Marchenko S. V., Moffat A. F. J., Vacca W. D., Côté S., Doyon R., 2002, *ApJ*, 565, L59
- Mastrodemos N., Morris M., 1999, *ApJ*, 523, 357
- Mauron N., Huggins P. J., 2006, *A&A*, 452, 257
- Mitsumoto M. et al., 2005, *Astron. Rep.*, 49, 884
- Monnier J. D., Tuthill P. G., Danchi W. C., 1999, *ApJ*, 525, L97
- Okazaki A. T., Owocki S. P., Russell C. M. P., Corcoran M. F., 2008, in Bresolin F., Crowther P. A., Puls J. eds, *Proc. IAU Symp. 250, Massive Stars as Cosmic Engines*. Cambridge Univ. Press, Cambridge, p. 133
- Pittard J. M., 1998, *MNRAS*, 300, 479
- Pittard J. M., 1999, in van der Hucht K. A., Koenigsberger G., Eenens P. R. J., eds, *Proc. IAU Symp. 193, Wolf-Rayet Phenomena in Massive Stars and Starburst Galaxies*. Astron. Soc. Pac., San Francisco, p. 386
- Pittard J. M., 2007, *ApJ*, 660, 141
- Pittard J. M., Corcoran M. F., 2002, *A&A*, 383, 636
- Pittard J. M., Dougherty S. M., 2006, *MNRAS*, 372, 801
- Pittard J. M., Stevens I. R., 1997, *MNRAS*, 292, 298
- Pittard J. M., Stevens I. R., Corcoran M. F., Ishibashi K., 1998, *MNRAS*, 299, L5
- Pittard J. M., Stevens I. R., Corcoran M. F., Gayley K. G., Marchenko S. V., Rauw G., 2000, *MNRAS*, 319, 137
- Pollock A. M. T., Corcoran M. F., Stevens I. R., Williams P. M., 2005, *ApJ*, 629, 482
- Rauw G., Sana H., Gosset E., Vreux J.-M., Jehin E., Parmentier G., 2000, *A&A*, 360, 1003
- Romero G. E., Okazaki A. T., Orellana M., Owocki S. P., 2007, *A&A*, 474, 15
- Stevens I. R., 1996, in Niemela V., Morrell N., Pismis P., Torres-Peimbert S., eds, *Rev. Mex. Astron. Astrofis. Ser. Conf. Vol. 5, Workshop on Colliding Winds in Binary Stars to Honor Jorge Sahade*. UNAM, Mexico, p. 61
- Stevens I. R., Blondin J. M., Pollock A. M. T., 1992, *ApJ*, 386, 265
- Tuthill P. G., Monnier J. D., Danchi W. C., 1999, *Nat*, 398, 487
- Tuthill P. G., Monnier J. D., Tanner A., Figer D., Ghez A., Danchi W., 2006, *Sci*, 316, 247
- Tuthill P. G., Monnier J. D., Lawrance N., Danchi W. C., Owocki S. P., Gayley K. G., 2008, *ApJ*, 675, 698
- van der Hucht K. A., 2001, *New Astron. Rev.*, 45, 135
- Walder R., Folini D., 2000, in Lamers H. J. G. L. M., Sapar A., eds, *ASP Conf. Ser. Vol. 204, Thermal and Ionization Aspects of Flows from Hot Stars: Observations and Theory*. Astron. Soc. Pac., San Francisco, p. 331
- Walder R., Folini D., 2002, in van der Hucht K. A., Herrero A., Esteban C., eds, *Proc. IAU Symp. 212, A Massive Star Odyssey, from Main Sequence to Supernova*. Kluwer, Dordrecht, p. 139
- Williams P. M., Dougherty S. M., Davis R. J., van der Hucht K. A., Bode M. F., Setia Gunawan D. Y. A., 1997, *MNRAS*, 289, 10
- Zhekov S. A., 2007, *MNRAS*, 382, 886

This paper has been typeset from a $\text{\TeX}/\text{\LaTeX}$ file prepared by the author.